Burns & Trauma, 2020, 8, tkaa036
doi: 10.1093/burnst/tkaa036
Research Article

Research Article

Co-Cr-Mo-Cu alloys for clinical implants with osteogenic effect by increasing bone induction, formation and development in a rabbit model

Jingzhu Duan[1], Yang Yang[2], Erlin Zhang[3] and Huan Wang[1,*]

[1]Department of Orthopaedic, Shengjing Hospital of China Medical University, No. 36 Sanhao Street, Heping District, Shenyang 110004, China, [2]Department of Ophthalmology, Shengjing Hospital of China Medical University, No. 36 Sanhao Street, Heping District, Shenyang 110004, China and [3]Key Laboratory for Anisotropy and Texture of Materials, Education Ministry of China, School of Materials Science and Engineering, Northeastern University, No. 3-11 Wenhua Road, Heping District, Shenyang 110819, China

*Correspondence. Email: spinecmu@126.com

Received 4 January 2020; Revised 12 February 2020; Editorial decision 18 August 2020

Abstract

Background: Co-Cr-Mo alloy has been widely used in clinical implants because of its excellent mechanical and anti-corrosion properties, but there is an urgent need to address its disadvantages, such as implant-related infections and implant loosening. We synthesized Co-Cr-Mo-Cu (Co-Cu) alloys with different Cu contents to modify implant performance to be suitable as a bone-compatible implant material.
Methods: Microstructure, phase content and mechanical properties of the Co-Cr-Mo alloy were characterized. Histological and immunohistochemical analyses were performed after implantation in rabbits. The experimental alloy was implanted on the lateral side of the lower tibial condyle and the tibial nodule.
Results: Phase content and mechanical properties revealed that the crystallographic structure and wear resistance were changed. Experimental implantation results demonstrated that osteogenic capability was markedly enhanced, ascribed to the excellent antibacterial and osseointegration capacities of Cu phases, and with the release of Cu ions. In particular, Co-Cu alloy containing 2 wt% Cu exhibited the best osteogenic performance among all samples.
Conclusions: The results indicated that osteogenic performance of the Co-Cr-Mo alloy could be enhanced by adding Cu. In particular, the Co-2Cu alloy exhibited the best properties according to both immunohistochemical and histological analyses. Our study not only provides deep insight into the osteogenic effect of Cu but presents a new Co-Cu alloy for clinical implants.

Key words: Co-Cr-Mu-Cu alloy, Cu ion, Osteogenic capability, Implantable operation, Clinical application

Highlights

- Co-Cr-Mo-Cu alloys with osteogenic performances and antibacterial properties for modifying bone-compatible implant properties
- The addition of Cu improves the clinical implant performance of Co-Cr-Mo alloys
- Co-Cr-Mo alloy with added 2 wt% Cu exhibits the best osteogenic performance among all alloys

© The Author(s) 2020. Published by Oxford University Press.
This is an Open Access article distributed under the terms of the Creative Commons Attribution Non-Commercial License (http://creativecommons.org/licenses/by-nc/4.0/), which permits non-commercial re-use, distribution, and reproduction in any medium, provided the original work is properly cited. For commercial re-use, please contact journals.permissions@oup.com

Downloaded from academic.oup.com/burnstrauma/article/doi/10.1093/burnst/tkaa036/6042489 by guest on 15 October 2026

Background

Co-Cr-Mo alloy has been widely used for clinical implants because of its excellent mechanical properties, durability and corrosion resistance [1–4]. However, the relatively low osseointegration performance could result in aseptic loosening and thus delay the postoperative recovery after implant operation [5–6]. Furthermore, infection can also occur after the installation of the implant, which is associated with the low antibacterial property of the Co-Cr-Mo alloy [7–9]. Therefore, it is important to develop a Co-Cr-Mo alloy that possesses both excellent osteogenic and antibacterial properties for clinical implant application.

For this reason, many studies have been reported using surface modification or element alloying to develop the implant properties of Co-Cr alloys. In particular, Cu has proved to be an excellent option in terms of both its antibacterial and osteogenic properties, according to recent researches [10–15]. It has been reported that Cu-bearing Ti alloy and Cu-bearing stainless steel exhibit excellent antibacterial properties [10, 14]. Furthermore, Hu *et al*. revealed that substituted Cu and Zn hydroxyapatite coating could enhance antibacterial properties [16]. Pullisaar *et al*. reported that the osteogenic effect could be modified by superficial TiO_2 coating [17]. However, the surface treatment could only take effect before abrasion and detachment occurs. Thus, an implantable alloy that could exhibit excellent antibacterial and osseointegration properties in its life cycle would be the ideal medical implant material.

In the present study, we synthesized Co-Cr-Mo-Cu alloys (Co-Cu) with different Cu contents (0, 2 and 4 wt%), designated as Co-0Cu, Co-2Cu and Co-4Cu, respectively. With Cu added to the 29Cr-6Mo alloy, the antibacterial and osseointegration properties were markedly enhanced, which was ascribed to released Cu ions acting as antibacterial and osteogenic substances in the body, according to the experimental results. These improved properties, compared to the original Co-Cr-Mo alloy, could further increase the stability and durability of implant materials. In particular, the Co-2Cu alloy exhibited the highest osteogenic effect among all alloys. Furthermore, the added Cu slightly modified the mechanical properties and promoted relatively high corrosion resistance [18]. The present study demonstrates a new Co-Cu alloy with significant antibacterial and osteogenic properties for clinical implants, and also provides insight into the osteogenic effect of Cu.

Methods

Preparation of Co-Cu alloys

Co-Cu alloys with 2 and 4 wt% Cu were synthesized by the investment casting method. The Co-Cu alloys were melted in a vacuum-induction furnace and then poured into the ceramic mold to prepare the Co-Cu alloy with a size of $140 \times 50 \times 30$ mm^3. This is the same method as the original Co-Cr-Mo alloy was prepared by, based on GB17100–1997 [19]. The alloy ingots were then cut into rod-like implants, 2 mm in diameter and 6 mm in length, for implantation.

Microstructure characterization

X-ray diffraction (XRD) was performed by Smaertlab (Rigaku, Japan) in the 2-theta range from 30° to 100° with Cu Kα ($\lambda = 0.154$ nm) incident radiation using the following test parameters: scan step of 4°/minute, voltage of 35 kV and current of 200 mA. Scanning electron microscopy (SEM) was carried out using a Hitachi S3400 microscope with an energy-scattering spectrum (EDS) (Inca, Oxford, U.K.). SEM samples with dimensions of $15 \times 15 \times 1$ mm were prepared. All alloy samples were first ground with SiC emery paper (1500 grit) and diamond grinding paste (1.5 μm). The alloy samples were then etched in a 5 wt% HCl solution for ~15 seconds with a voltage of 5 V to expose the metallographic structures.

Mechanical properties

Microhardness was tested on a HVS-1000 microhardness meter (Huayin, China) with a 200-g test load and the holding time was 10 seconds. For each alloy sample, five different areas were randomly chosen, and the result was an average value with standard deviation ($x \pm y$, Table 4). Tensile samples were prepared from the original alloy ingots, with dimensions of $30 \times 6 \times 2$ mm, and were pre-prepared with SiC emery paper. Microhardness was determined using a universal testing machine with a speed of 1 mm/min. Wear resistance was characterized by a pin-on-disk test using the TRB tribometer (Nanovea, U.S.A.) with a 6 mm-diameter Al_2O_3 ball. The disk speed was set at 350 rpm and the pin was mounted with 5 N. The rotation radius was 4 mm and the analysis time was 2 hours. The sample was cleaned with distilled water and ethanol and then dried in ambient air before the test. All tests were done three times to obtain an average value. The abrasion loss property was determined with a detector on the basis of the wear trace.

Ion release

Different alloy samples were ground with SiC emery paper and then cleaned with an ultrasonic washer in ethanol for 10 minutes. The samples were then rinsed with water. To characterize the ion release, the samples were immersed in 0.9 wt% NaCl solution with a surface area-to-volume ratio of 1.5 cm^2/ml for ~1 day. Cu ion concentration in the solution was determined by inductively coupled plasma mass spectrometry (ICP-MS) (Optima 5300DV, Perkin Elmer, U.S.A.) with a sensitivity of 5 μg/L (5 ppb).

Implantation

Thirty New Zealand white rabbits of either gender, weighing 2.5–3 kg, were randomly grouped and fed in separate cages according to Regulations for the Administration of Affairs Concerning Experimental Animals. The rabbits were regularly observed. Immunohistochemistry assays were divided into four groups according to time in weeks (1, 2, 3 or 4 weeks), with 3 rabbits in each group. Histological analysis

Downloaded from academic.oup.com/burnstrauma/article/doi/10.1093/burnst/tkaa036/6042489 by guest on 15 October 2026

and fluorescence labeling assays were divided into three groups in terms of time in weeks (4, 8 or 12 weeks), with 3 rabbits in each group. First, Co-Cu alloy and pure Ti implants were autoclaved before implantation and a longitudinal incision of ~3–4 cm was made on the lateral side of the lower tibial condyle and the tibial nodule in the rabbits. Those receiving the Ti alloy implant served as the control group in this study, because Ti alloy is the most widely used implant material. The soft tissue was separated into the periosteum and stripped. Afterwards, a 1.8 mm hold was drilled and the cylindrical alloy samples were implanted. The tibial tips on the experimental side and the bones were cut with a saw at 1 cm from the proximal and distal ends of the protruding tips of the implants and all soft tissue attachments were removed to prepare the bone segments. The locations of the Co-Cu and Ti implants were recorded and the bone segments were examined by X-ray at 4w, 8w or 12w to observe the osseointegration of implants.

Detection indices

The tibial bone segments of experimental rabbits in the 1-, 2-, 3- and 4-week groups were decalcified with 4% methanol in phosphate-buffered saline (PBS). Complete decalcification was indicated by the ability to easily prick the bone tissue with 1-ml needle tips without any resistance. The bone segments were then embedded and IGF-1 (insulin-like growth factor) and/or BMP-2 (bone morphogenetic protein-2) were determined using immunohistochemistry kits [20–21]. The sections were observed under the microscope and then analysed by ImageJ (NIH, U.S.A.). Enzyme-linked immunosorbent assay (ELISA) was carried out to determine the content of IGF-1 and/or BMP-2 in the local area around the alloy.

Histological analysis

Bone segments were pre-prepared by soaking in 4% methanol, alcohol dehydration and stained with Masson trichrome. The samples were observed under a light microscope. Bone–implant contact (BIC) was calculated via NIS-Elements AR software (Nikon, Japan), in which the (length of direct contact between the bone and the implant)÷(interface length) × 100% = BIC. In addition, the bone segments of the experimental groups were immersed in 5% glutaraldehyde in PBS, dehydrated with alcohol and embedded in resin to study the distance between the two fluorescence marker lines. The samples were observed with a fluorescence confocal microscope and mineral apposition rate (MAR) was calculated as follows: MAR = $d_F/t_F \times 100\%$, where d_F represents the average value of the distance between the two fluorescence marker lines on the surface of trabecular bone and t_F represents the interval time of fluorescence marking [22–23].

Statistical analysis

All experiments were carried out in triplicate, and the values are presented as the mean ± standard deviation. For the ion release experiments, the multiple comparisons of each group were made using one-way analysis of variance (ANOVA). For the quantitative data of BMP-2 and IGF-1 expression, BIC and MAR, data between groups and different time points were analysed using two-way ANOVA. A value of $p < 0.05$ was considered statistically significant.

Results

Microstructure

Co-Cu alloys were synthesized by the vacuum-melting method, in which the elemental composition of the different alloys were characterized by X-ray fluorescence spectrometry and ICP-MS, as shown in Tables 1 and 2. To investigate the phase composition of the different alloys, XRD patterns were introduced, as shown in Figure 1. The microstructures of the different alloys were characterized by SEM at a 20 kV. SEM images and the corresponding element distribution images (EDS mapping) of the three Co-Cu alloys are exhibited in Figure 2, in which Co, Cr, Mo and Cu are indicated in different colors. In addition, it can be seen that the different

Table 1. Chemical composition of different Co-Cu alloys (wt%)

Alloys	Cr	Mo	Fe	Ni	Si	C	Mn	Cu	Co
Co-0Cu	29	6	0.8	0.5	0.6	0.2	0.6	0	Balance
Co-2Cu	29	6	0.8	0.5	0.6	0.2	0.6	1.9	Balance
Co-4Cu	29	6	0.8	0.5	0.6	0.2	0.6	3.8	Balance

Table 2. Chemical composition of different Co-Cu alloys (parts per million)

Alloys	Cr	Mo	Fe	Ni	Mn	Cu	Co
Co-0Cu	28.5	6.1	0.7	0.2	0.7	0.2	63.6
Co-2Cu	29.2	5.7	0.8	0.4	0.8	2.2	60.9
Co-4Cu	28.7	6.5	0.8	0.3	0.7	3.9	59.1

Downloaded from academic.oup.com/burnstrauma/article/doi/10.1093/burnst/tkaa036/6042489 by guest on 15 October 2026

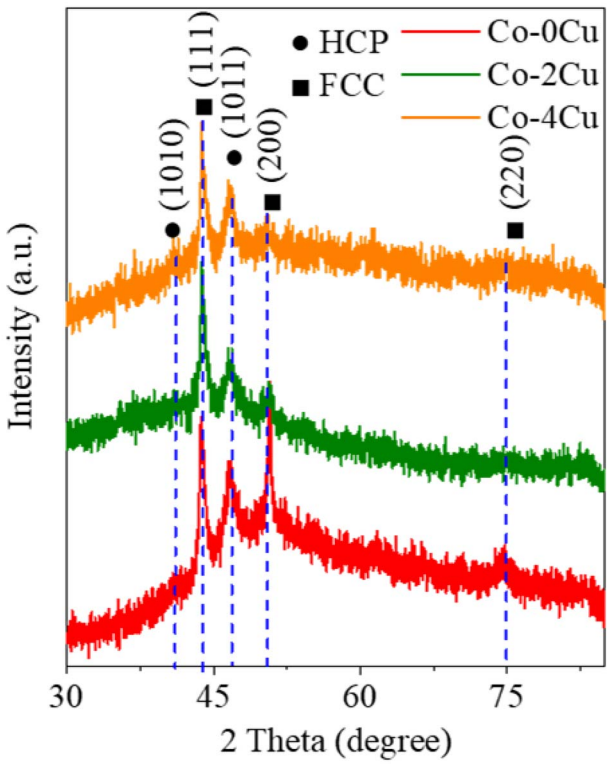

Figure 1. Phase characterization of three different Co-Cu alloys (by X-ray diffraction), where it can be seen that the hexagonal closepacked structure (HCP) and face center cubic (FCC) phases and the FCC γ-Co phase could modify ductility and deformability of Co-Cu alloys

alloy samples exhibited different surface microstructures, which were associated with different Cu content. The element content of different Co-Cu alloys was confirmed by EDS characterization, as shown in Table 3. X-ray photoelectron spectroscopy (XPS) analysis, which shows the element content of Co-Cu alloys, is presented in Figure 3, exhibiting the surface element constitutions of the different Co-Cu alloys.

Mechanical properties

To investigate the mechanical properties of different Co-Cu alloys, microhardness, yield strength (YS) and ultimate tensile strength (UTS) were characterized and are summarized in Figure 4 and Table 4. With increasing Cu content, the microhardness of Co-Cu alloys was reduced from 296 to 276 HV with the enhancement of YS and UTS performance. In particular, when Cu content was increased to 4 wt%, the alloy exhibited the greatest strengths, both YS and UTS, and elongation among all Co-Cu alloys. The friction coefficient and abrasion loss of the Co-Cu alloys are shown in Figure 5. Co-0Cu alloy exhibited a friction coefficient of 0.577 and an abrasion loss of 8.31×10^{-5} mm^3/Nm. Friction coefficient and abrasion loss increased to 0.624 and 1.05×10^{-4} mm^3/Nm in Co-4Cu alloys, which could indicate that the added Cu slightly reduced the wear resistance of Co-Cr-Mo alloy [24–26].

Ion release

The ion release results for the Co-Cu alloys in 0.9% NaCl solution after 1 day of immersion are displayed in Figure 6. It can be noted that, with increasing Cu content in the Co-Cu alloys, the Cu ion concentration increased to 20.7 μg/L ($p > 0.05$) in the Co-2Cu alloy, but for the Co-4Cu alloy, it increased to 485 μg/L ($p < 0.05$). On the contrary, Cr and Co ion concentrations exhibited the opposite change: with increasing Cu content, both Co and Cr content decreased simultaneously.

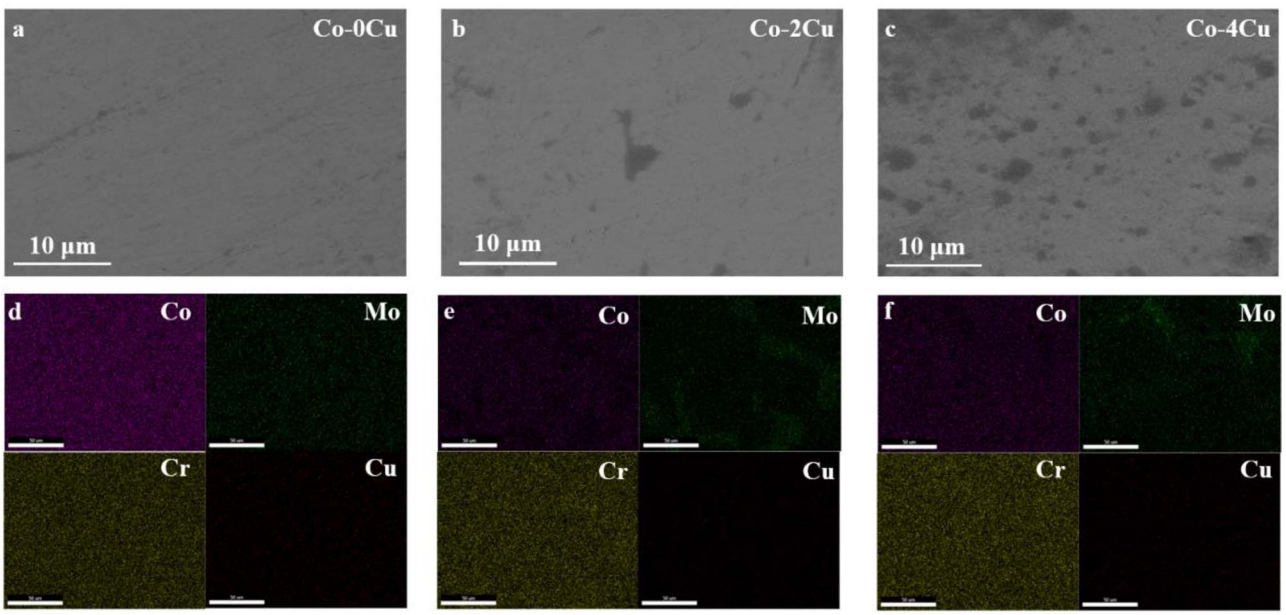

Figure 2. Microstructure of Co-Cu alloys with different Cu content. The second phase structure showed a clear difference. **(a–c)** High resolution-scanning electron microscope images of different Co-Cu alloys. **(d–f)** The corresponding energy-scattering spectrum mapping images, scale bar: 50 μm

Downloaded from academic.oup.com/burnstrauma/article/doi/10.1093/burnst/tkaa036/6042489 by guest on 15 October 2026

Table 3. Energy-scattering spectrum analysis of different alloys at different random points (at%)

Elements	Point A			Point B			Point C		
	Co-0Cu	Co-2Cu	Co-4Cu	Co-0Cu	Co-C2u	Co-4Cu	Co-0Cu	Co-2Cu	Co-4Cu
Co	46.90	58.44	58.49	64.18	59.37	58.87	47.23	57.98	59.05
Cr	40.61	34.52	33.11	32.55	34.28	32.98	40.47	32.87	32.89
Mo	12.50	4.42	3.89	3.25	4.04	4.02	12.30	3.84	3.91
Cu	0.05	1.39	3.43	0.04	1.28	3.04	0.12	4.35	3.25

Table 4. Microhardness and tensile properties of different Co-Cu alloys

Alloys	Microhardness, HV	Tensile strength, MPa		Elongation, %
		0.2% YS strength	UTS	
Co-0Cu	296.56 ± 27.61*	415.72 ± 13.22*	503.98 ± 35.18*	12.5 ± 0.9*
Co-2Cu	281.71 ± 25.15*	423.42 ± 15.89*	490.64 ± 32.11	11.3 ± 3.1
Co-4Cu	276.33 ± 26.64	438.91 ± 24.44*	603.25 ± 26.16*	14.9 ± 1.1

*$p < 0.05$

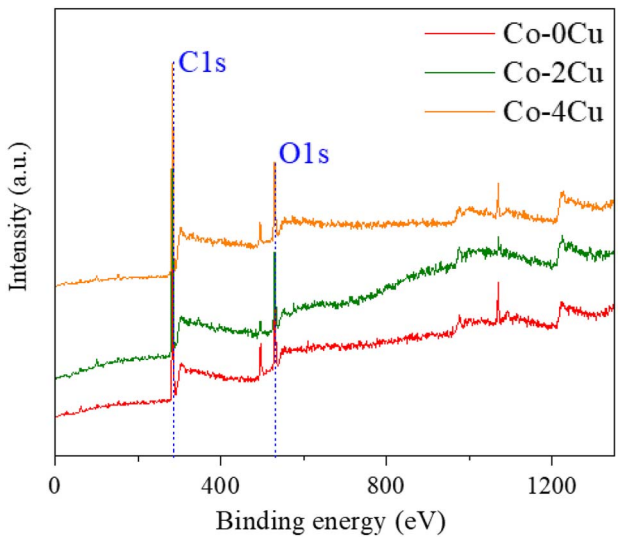

Figure 3. Element characterizations (X-ray photoelectron spectroscopy) of three different Co-Cu alloys. The C1s and O1s peaks observed were ascribed to the surface segregation behavior of the Co-Cu alloys

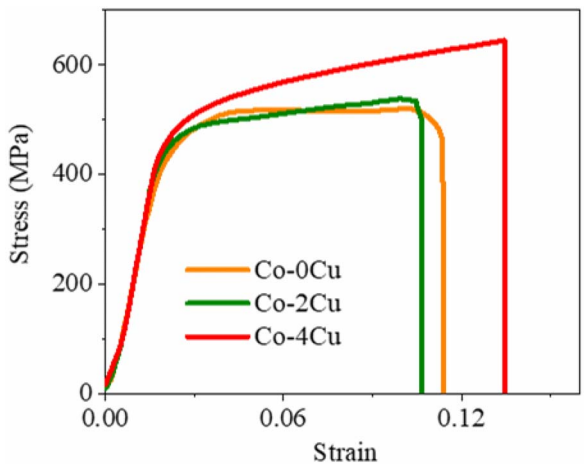

Figure 4. Tensile stress–strain curves of the different Co-Cu alloys. The Co-Cu alloys showed improved ductility

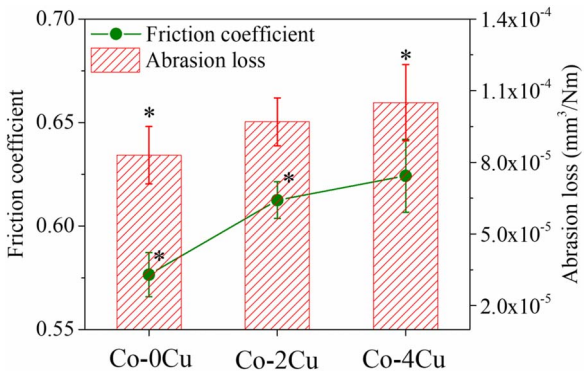

Figure 5. The friction coefficient and abrasion loss of the different Co-Cu alloys. The enhancement of abrasion loss performance was ascribed to the large carbide phases and inhomogeneous element distribution (*$p < 0.05$)

Implant experiment

To investigate the osseointegration capacity of Co-Cu alloy, an animal implant experiment was designed as shown in Figure 7a. Rod-like Co-0Cu, Co-2Cu, Co-4Cu and Ti (control group) alloys were implanted in rabbits. All experimental animals were alive with well-healed surgical incisions and no infection after implantation. The surfaces of implants were covered with different amounts of bone callus, and the implant was in close contact with the bone in all groups, as shown in Figure 7b. With the implantation time increased to 4 weeks, a small amount of new bone callus formed, which indicated that an osseous connection had begun to occur between the implant alloy and bone tissue. At 8 weeks, lamellar bone, which showed increasing cortical bone thickness and amount of cancellous bone, and cortical bone could be observed around the implant alloy, confirming the further integration of bone tissue and implant alloy. Finally, at

Downloaded from academic.oup.com/burnstrauma/article/doi/10.1093/burnst/tkaa036/6042489 by guest on 15 October 2026

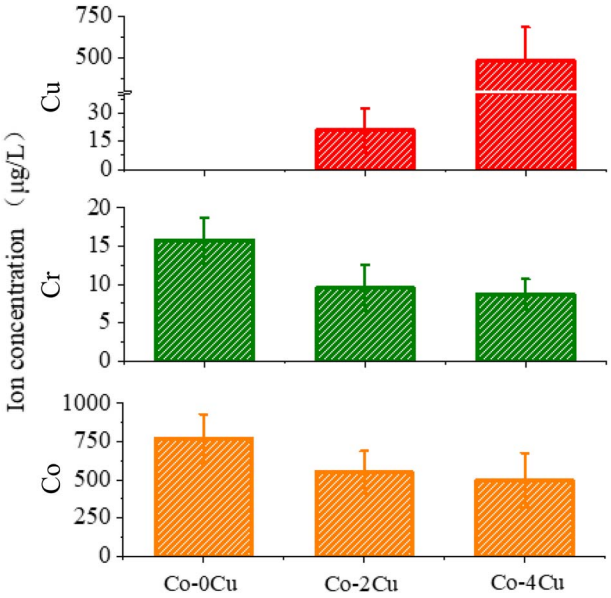

Figure 6. Ion release of Co-Cu alloys in 0.9% NaCl solution after 1-day immersion. Co, Cr and Cu were detected with all Co-Cu alloys. The ion concentrations were much lower than reported values, which makes it less likely that the released ions would result in cell toxicity

12 weeks, the contact surface between bone and implant alloy was surrounded by a large amount of lamellar bone, and the cortical bones on both sides were filled with new bone with a density close to that of normal mature bone tissue, indicating that an excellent osseous connection had appeared between the implant alloy and bone tissue.

Immunohistochemistry

In the clinical implant operation, growth factors played an important role in bone healing and tissue repair. To characterize the osteogenic performance of the different Co-Cu alloys, BMP-2 and IGF-1 were studied as markers for osteoblasts, as shown in Figure 8–9. BMP-2 has been shown to be a multifunctional growth factor, which can induce mesenchymal cells to differentiate into cartilage cells and thereby form new bone, with components including osteoblasts, osteoclasts and bone marrow tissue [27–29]. IGF-1 can dynamically balance the metabolic process of cartilage cells, directly inducing the synthesis of DNA and RNA in osteoblasts, participating in bone remodeling and bone metabolism for bone resorption [30–31]. Both BMP-2 and IGF-1 showed increased expression after the implant operation, and the differences between the

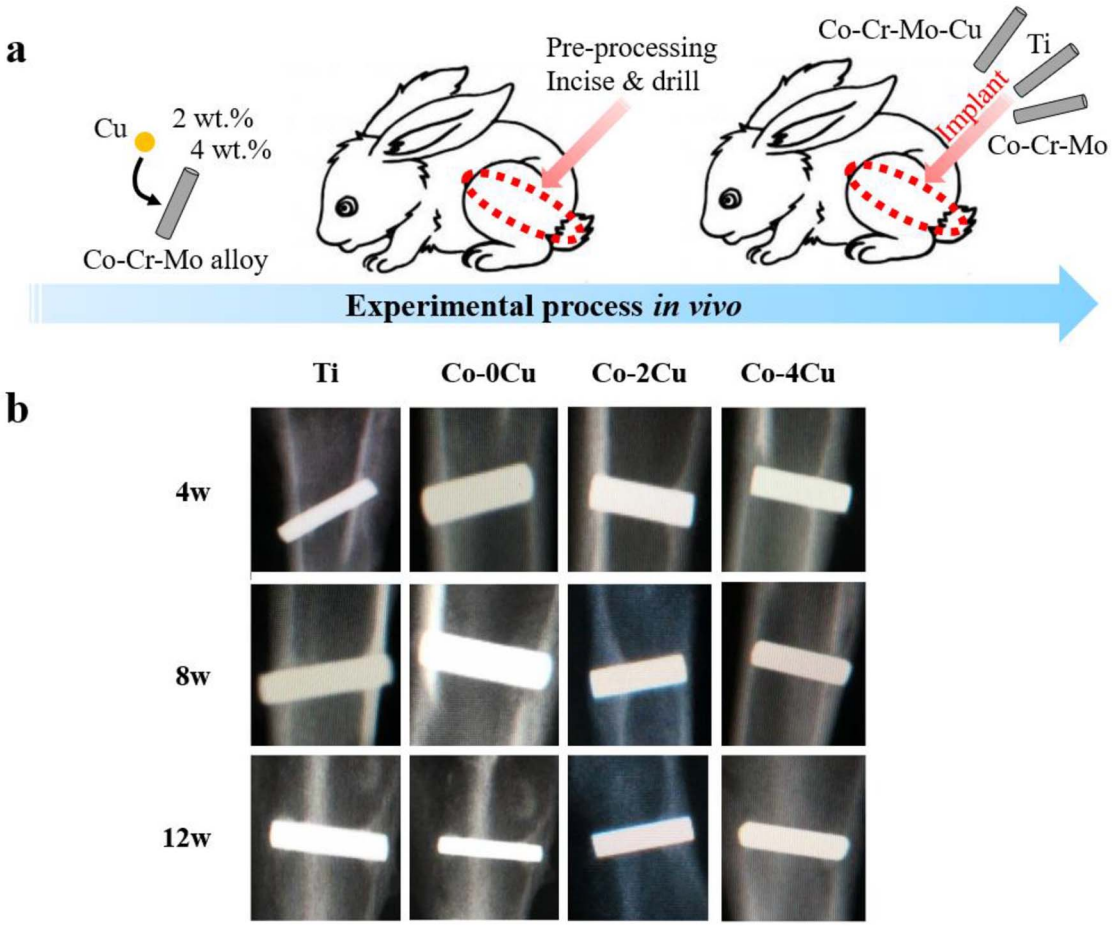

Figure 7. The osseous connection between the implant alloy and bone tissue. **(a)** Scheme of the corresponding animal experiment. **(b)** Radiologic examination for implant alloy and bone tissue at 4, 8 and 12 weeks. It can be seen that, in many cases, the lamellar and cortical bone is filled with new bone tissue and the density of this is close to that of mature bone

Downloaded from academic.oup.com/burnstrauma/article/doi/10.1093/burnst/tkaa036/6042489 by guest on 15 October 2026

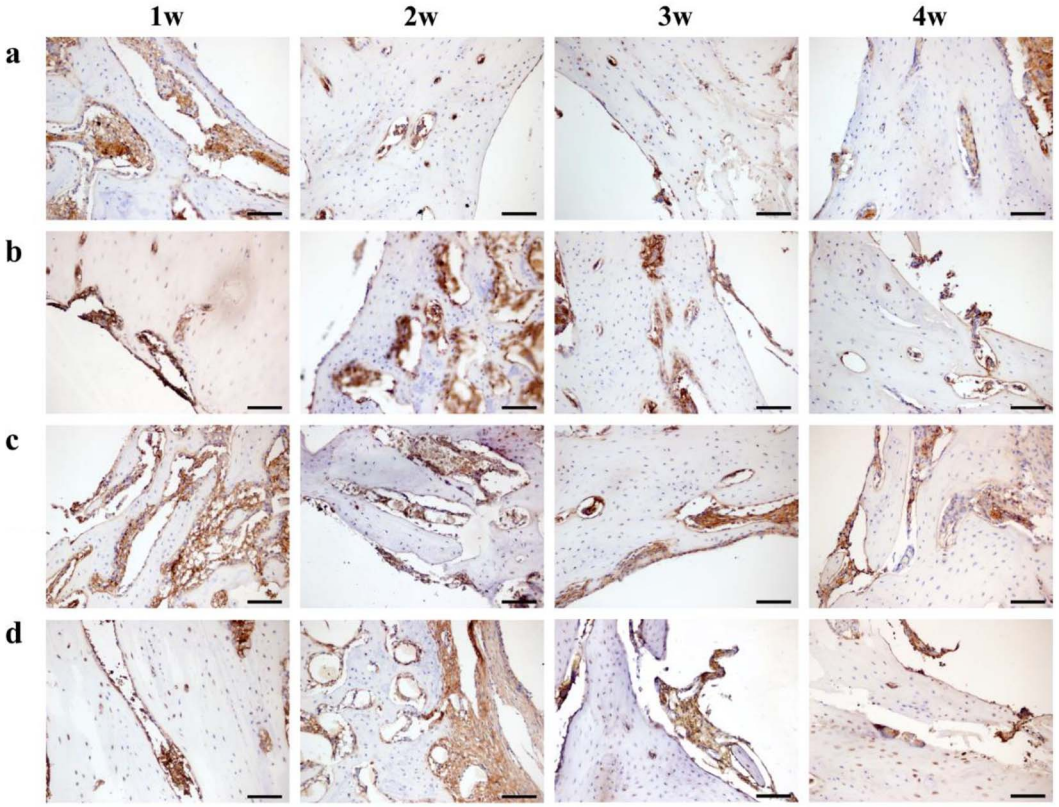

Figure 8. Immunohistochemical analysis of Co-Cu alloy implantation (bone morphogenetic protein-2), which might reflect the mesenchymal cells differentiating into cartilage cells and thereby forming new bone, with a composition including osteoblasts, osteoclasts and bone marrow tissue (scale bar: 20 μm) **(a)** Ti alloy; **(b)** Co-0Cu alloy; **(c)** Co-2Cu alloy; **(d)** Co-4Cu alloy

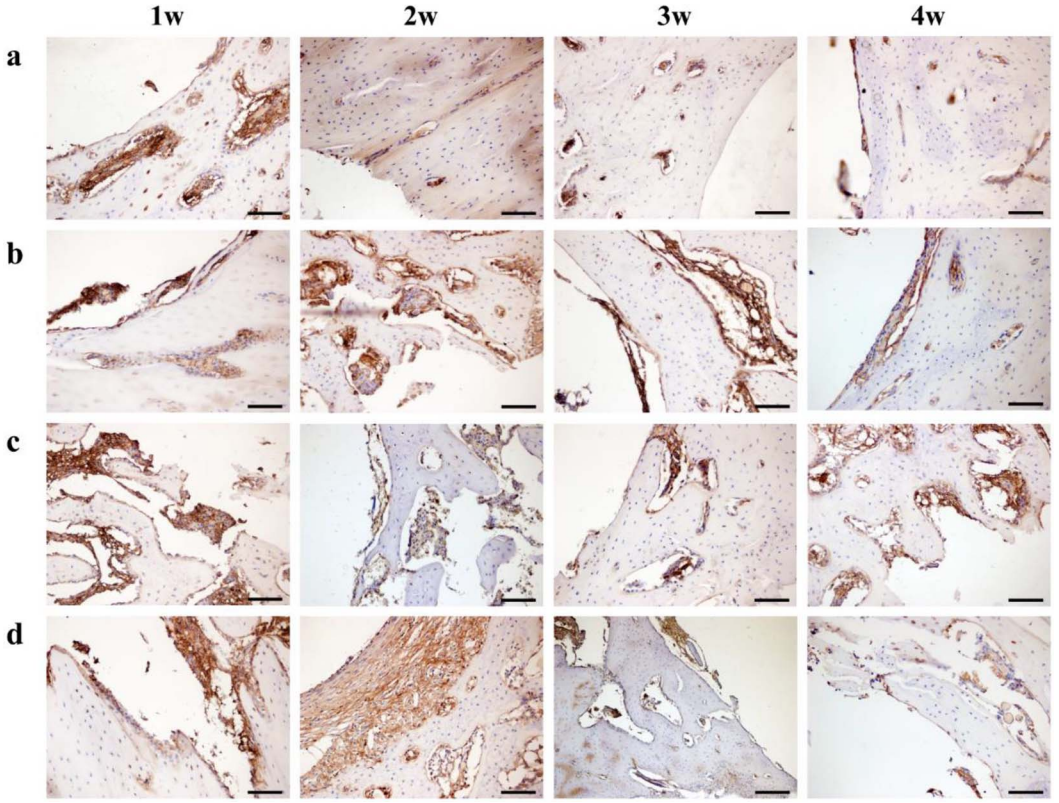

Figure 9. Immunohistochemical analysis of Co-Cu alloy implantation (insulin-like growth factor), which could reflect the synthesis of DNA and RNA in osteoblasts, participating in bone remodeling and bone metabolism for bone resorption (scale bar: 20 μm). **(a)** Ti alloy; **(b)** Co-0Cu alloy; **(c)** Co-2Cu alloy; **(d)** Co-4Cu alloy

Downloaded from academic.oup.com/burnstrauma/article/doi/10.1093/burnst/tkaa036/6042489 by guest on 15 October 2026

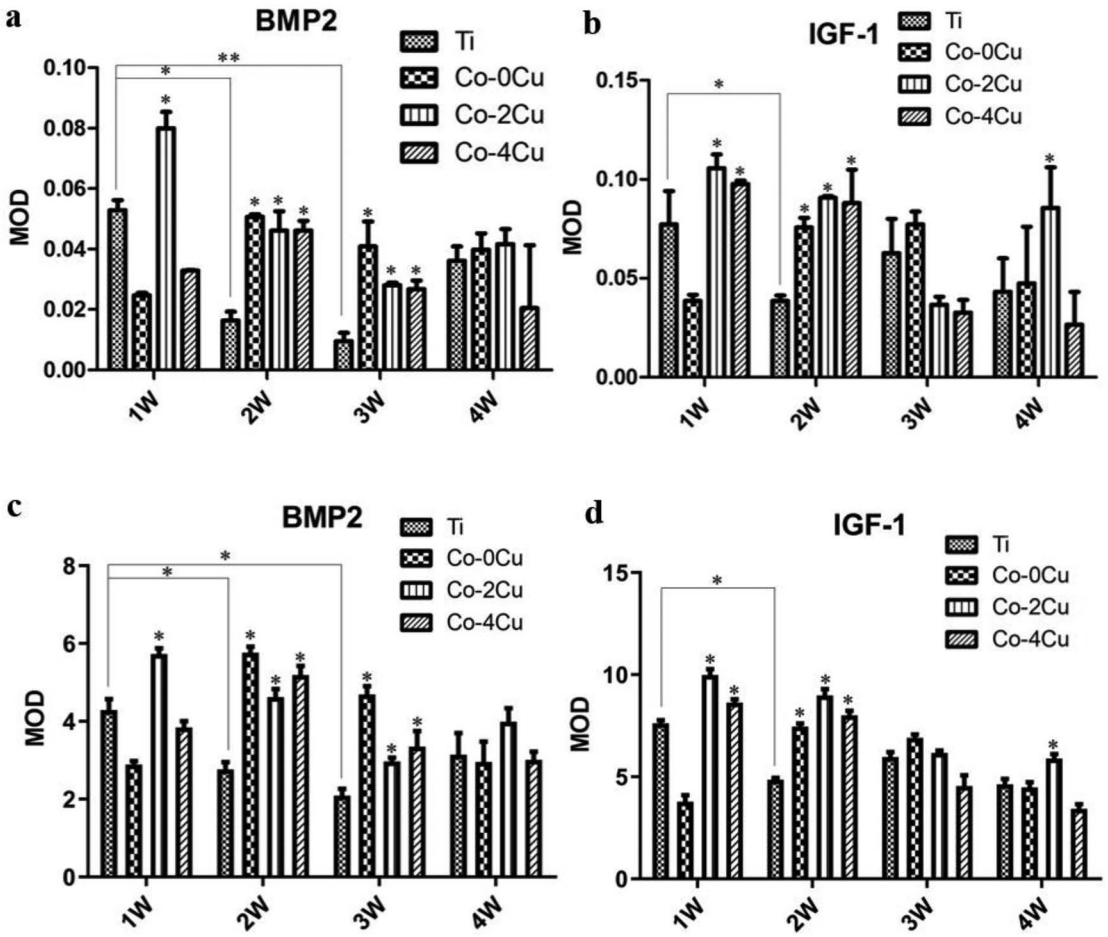

Figure 10. The average optical densities for: **(a)** bone morphogenetic protein-2 (BMP-2) for Ti and Co-Cu alloys in the 1-, 2-, 3- and 4-week groups; and **(b)** insulin-like growth factor (IGF-1) for Ti and Co-Cu alloys in the 1-, 2-, 3- and 4-week groups. IGF-1 and BMP-2 expression measured by enzyme-linked immunosorbent assay: **(c)** BMP-2 for Ti and Co-Cu alloys in 1-, 2-, 3- and 4-week groups; and **(d)** IGF-1 for Ti and Co-Cu alloys in 1-, 2-, 3- and 4-week groups ($*p < 0.05$; $** p < 0.01$)

alloys are displayed in Figure 10a, b. Accurate quantification of IGF-1 and BMP-2 expression in the local area around the alloy was achieved by ELISA and is shown in Figure 10c, d.

Histological analysis

Histological analysis of different bone samples was by Masson trichrome staining. After staining, the bone trabeculae showed a blue-stained structure of varying depth. The bone cells appeared as irregular white dots and fibrous tissue remained pink-stained, while new bone was not stained, as shown in Figure 11. Compared with the osteogenic activity among all implant samples, Co-2Cu alloy exhibited thicker and denser fibrous bone tissue and thus showed an optimal histocompatibility behavior. The BIC of each alloy is shown in Figure 12a [32–33]. The value, which exceeded 50% at 4 weeks and reached 80% at 12 weeks, demonstrated osseointegration and early stability between bone and implant. The Co-2Cu alloy exhibited the highest BIC values among all implant samples, thus demonstrating that it had a modified osteogenic performance.

MAR characterization

The histological analysis could directly determine bone differentiation, position and the levels of various growth factors, and also the bone mineralization capacity. The mineralization trend and mineralization rate could further evaluate the osteogenic properties of the different alloys, which could only be determined using fluorescent staining. By fluorescent labeling of the position of bone deposition at different time points and different directions, the bone formation distance in this period was measured. In addition, MAR was calculated by software analysis, as shown in Figure 13 [34–36]. Meanwhile, the MAR results also verified the compatibility relationship of the different Co-Cu alloy with bone tissue, as shown in Figure 12b.

Downloaded from academic.oup.com/burnstrauma/article/doi/10.1093/burnst/tkaa036/6042489 by guest on 15 October 2026

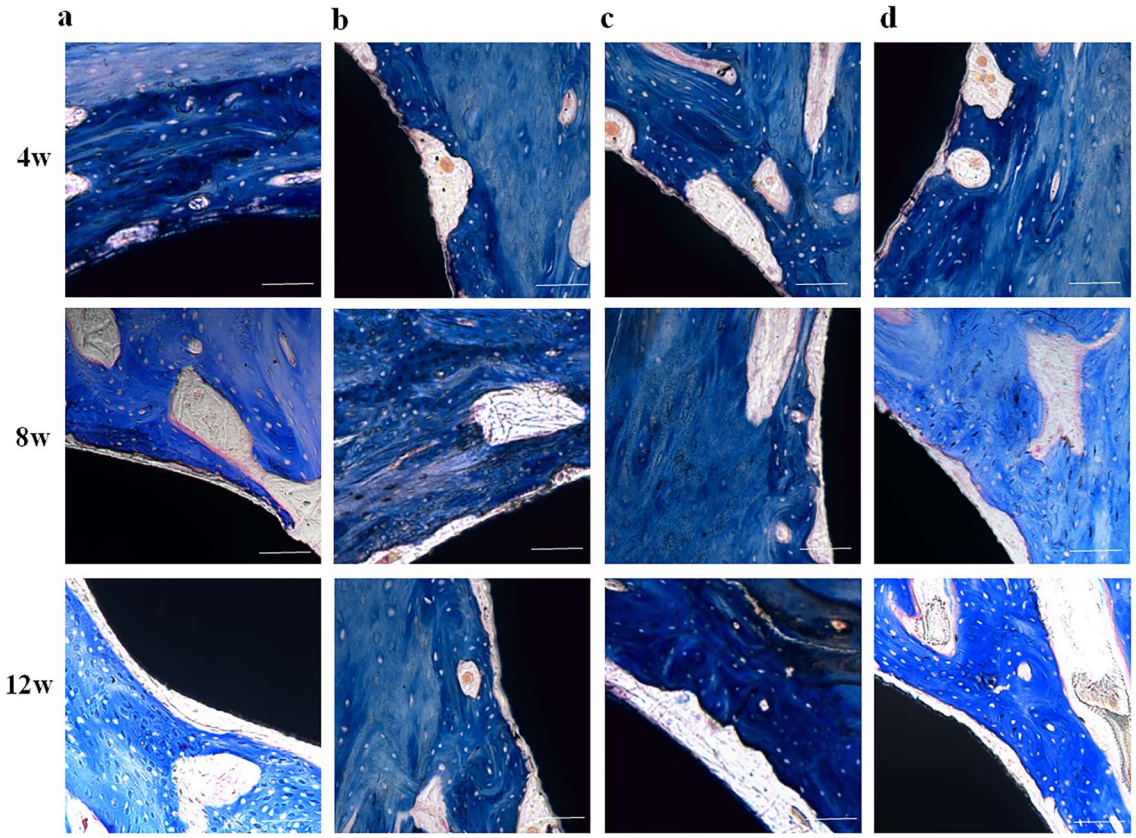

Figure 11. Histological structures with Co-Cu alloys. After Masson's trichrome staining, bone trabeculae exhibited a blue-stained structure of varying depth. Bone cells appear as irregular white dots, fibrous tissue is pink-stained and new bone is not stained (scale bar: 100 μm). **(a)** Ti alloy; **(b)** Co-0Cu alloy; **(c)** Co-2Cu alloy; **(d)** Co-4Cu alloy

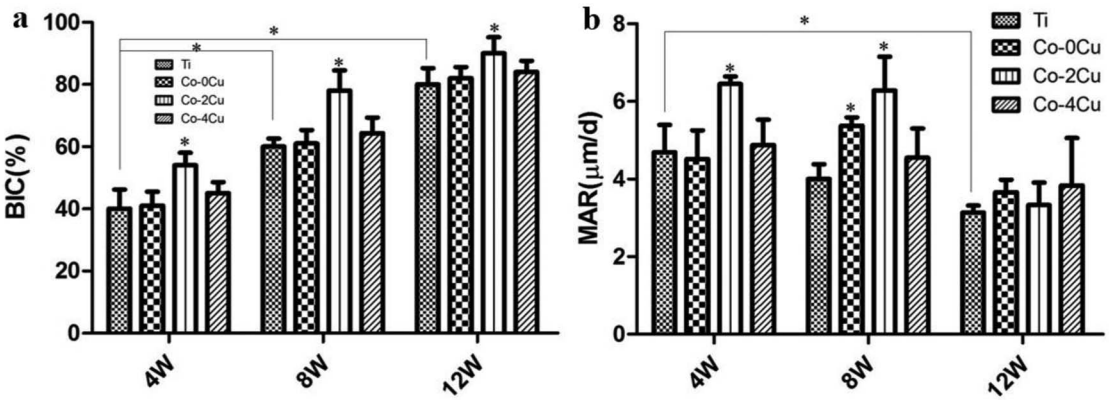

Figure 12. Statistical results of bone–implant contact (BIC) and mineral apposition rate (MAR) characterization for the different alloys. **(a)** BIC measurements for Ti and Co-Cu alloys in the 4-, 8- and 12-week groups. **(b)** MAR measurements for Ti and Co-Cu alloys in the 4-, 8- and 12-week groups ($*p < 0.05$; $** p < 0.01$)

Downloaded from academic.oup.com/burnstrauma/article/doi/10.1093/burnst/tkaa036/6042489 by guest on 15 October 2026

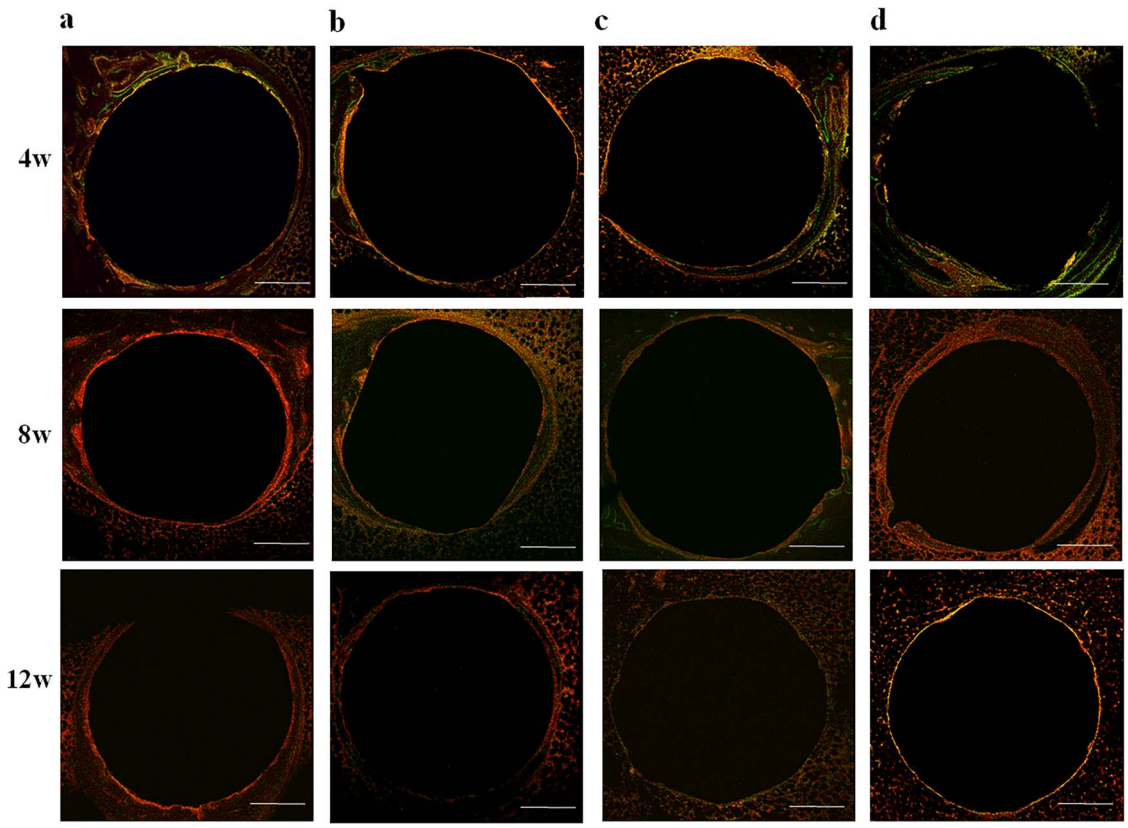

Figure 13. Mineral apposition rate characterization of the different Co-Cu alloys. Using fluorescent labeling of the position of bone deposition at different time points and different directions, the bone formation distance in this study period was measured (scale bar: 500 μm). **(a)** Ti alloy; **(b)** Co-0Cu alloy; **(c)** Co-2Cu alloy; **(d)** Co-4Cu alloy

Discussion

According to the XRD results, both the FCC γ-Co phase and the HCP ε-Co phase existed in all Co-Cu alloys [37–38]. In particular, with increasing Cu content, the ratio between the face center cubic (FCC) and hexagonal closepacked structure (HCP) phase exhibited a synchronous change. Furthermore, the Cu phase was not detected in the XRD pattern for all three Co-Cu samples. Generally, Co alloy always contains two kinds of crystal structures: the FCC γ-Co phase at high temperature (>~1173 K) and the HCP ε-Co phase at low temperature. It should be noted that the FCC γ-Co phase is always desired in Co alloys because of modified ductility and deformability. Corresponding studies, such as the addition of nitrogen, carbon and nickel have been proven to react to the transformation from the HCP phase to the FCC phase [39–41]. For this reason, XRD characterization indicates that the γ-Co phase in Co-Cu alloys is significantly increased by adding Cu, which means that Cu also has the ability to stabilize the FCC Co phase.

The microstructure consisted of a Co matrix and secondary phase [42], and the corresponding secondary phase influenced the mechanical properties of the Co-Cu alloys, which is discussed below. As the EDS mapping image shows, the different elements are indicated in different colors. Co, Cr and Cu can be observed in the color map. Moreover, Cu was also detected in the Co-0Cu alloy, which was ascribed to test error during EDS characterization. In addition, as the EDS result showed, Cu content exhibited an approximate value randomly, confirming that Cu had been uniformly dissolved in the Co-Cu alloy. For the Co-Cu alloys, it can be noted that Cu has a maximum solid solubility of 20.9 wt% in Co at 1367°C in the Co-Cu phase diagram, and, at room temperature, Cu and Co are nearly undissolved [18]. In addition, any intermetallic compound could be found between Co and Cu. During the decrease in temperature, the Cu phase and carbide phase precipitated from the melting or matrix, leading to the concentration of the Cu phase, which could result in the fluctuation of elemental content, as shown in Table 3. In XPS characterization, the results showed the existence of the carbide phase at the surface of the different Co-Cu alloys. According to the survey spectra of three different Co-Cu alloys, only the C1s and O1s peak could be observed and the Co, Cr, Mo and Cu were almost undetected. For this reason, it is hard to determine the valence of the different elements. The corresponding results indicated that element segregation occurred in all alloys during the preparation process, which could had led to performance changes in the following tests, and this might be further investigated in follow-up studies.

According to mechanical properties and microstructure, it could be concluded that Cu promotes the transforma-

Downloaded from academic.oup.com/burnstrauma/article/doi/10.1093/burnst/tkaa036/6042489 by guest on 15 October 2026

tion from the HCP ε-Co phase to the FCC γ-Co phase, which could enhance the mechanical performance of Co-Cu alloys. Moreover, increased Cu content improved the ductility of Co-Cu alloys. Also, in clinical implant application, excellent wear resistance performance is an important index and high wear resistance is often desired for Co-based biomaterials. In Table 4, it can be seen that the friction coefficient and abrasion loss increased with increasing Cu content. In other words, this means that added Cu deteriorated the wear properties of Co-Cu alloys. Combined with the HV characterizations in Table 4, it can be observed that added Cu reduced the microhardness of Co-Cu alloys and thus would lead to the corresponding enhancement of abrasion loss performance. The corresponding mechanical properties could be attributed to the as-cast condition of Co-Cu alloy in this study, such condition with large carbide phase and the inhomogeneous element distribution could influence the microstructures and thus reduce the mechanical performance. Therefore, it is necessary to find an effective way for optimizing the wear properties of Co-Cu alloys [31, 43].

Ion release, which included Co, Cr and Cu, was detected for all Co-Cu alloys, as shown in Figure 6. It has been reported that the TC50 concentrations of these three ions for MO3.13 cells are 215.5, 2083.7 and 178.8 μM, respectively. For human gingival fibroblasts, the TC50 concentrations of these three ions are about 705.8, 1971 and 344 μM, respectively [44]. With our alloys, the maximum concentrations of these three ions were 12.7, 0.3 and 8.5 μM, respectively. Therefore. the ion concentrations here were much lower than the previously reported values, which would result in the released ions not causing cell toxicity. In addition, the antibacterial properties of the Co-Cu alloys were systematically studied in our previous work [18] and it was concluded that the antibacterial properties of the Co-Cr-Mo alloys were markedly modified by Cu, which was associated with the tiny Cu phase at the grain boundary and inner grain and the Cu ion release from the Co-Cu alloy.

Immunohistochemistry results showed high expression of both BMP-2 and IFG-1 in the first 2 weeks after implantation, which indicated the active formation of new bone in the early stage. Following this, the proportion and amount of new bone decreased—this is ascribed to increased mineralization of new bone as time progressed. In particular, it can be observed that the Co-2Cu alloy showed a significant improvement in both BMP-2 and IGF-1 expression among all samples, which could be associated with an appropriate Cu ion release rate, thereby promoting bone induction, formation and development.

Histological analysis showed that 4 weeks after implantation, collagen fibers had been generated on the black defect near the implant border. A thin osteoblast layer was distributed discontinuously and a small osteoid was randomly produced. The new bone extended along the surface of implants with a relatively small contact area. At 8 weeks, the new bone number increased significantly. Around new trabecular bone, osteoblasts were neatly arranged in the bone interface. These osteoblasts were distributed continuously in the multilayer and connected with the implant material. At 12 weeks, a large amount of new bone tissue filled the interface of the implant material. The boundary between the new bone tissue and the original natural bone disappeared. The trabecular bones in the figure widened and their number continued increasing. In addition, a part of the woven bone at the periphery of the interface began to convert to lamellar bone, which appeared as an unstained fibrotic bone band. The Co-2Cu alloy exhibited the highest BIC values among all implant materials and thus demonstrated that it had a modified osteogenic performance.

In MAR characterization, the new bone tissue, which was far from the implant, was fluorescently labeled as a circular light bond at 4 weeks. The main components were stromal cells, fibrous tissue, collagen tissue and a small amount of osteoid and fibrotic bone. At 8 weeks, the distance between the two fluorescent bonds and implant decreased; the special mass of bone formed a light ring structure and bone tissue began to form on the side of the implant surface. At 12 weeks, different sizes of light rings and bands appeared around the implant and a large number of new bones formed, which almost completely fused with natural bone tissue. In addition, the distance between the light bands disappeared. These results showed that each Co-Cu alloy exhibited excellent osteogenic capability compared with Ti alloy, and the Co-2Cu alloy showed the best performance among the Co-Cu alloys.

Conclusions

In summary, we demonstrated an effective Co-Cu alloy for clinical implant application. The experimental material results revealed that Cu accelerated the formation of the γ-Co phase and had a slight influence on mechanical properties. The experimental implant results indicated that osteogenic performance could be effectively modified by adding Cu. In particular, the Co-2Cu alloy exhibited the best properties on the basis of BMP-2, IGP-2, BIC and MAR measurements. We presented here not only a novel Co-Cu alloy for implant application but provided deep insight into the osteogenic performance of Cu-containing implants.

Abbreviations

Co-Cu: Co-Cr-Mo-Cu alloy; XRD: X-ray diffraction; SEM: scanning electron microscopy; EDS: energy-scattering spectrum; ICP-MS: inductively coupled plasma mass spectrometry; PBS: phosphate-buffered saline; IGF-1: insulin-like growth factor; BMP-2: bone morphogenetic protein-2; ELISA: enzyme-linked immunosorbent assay; BIC: bone–implant contact; MAR: mineral apposition rate; ANOVA: analysis of variance; XPS: X-ray photoelectron spectroscopy; YS: yield strength; UTS: ultimate tensile strength

Downloaded from academic.oup.com/burnstrauma/article/doi/10.1093/burnst/tkaa036/6042489 by guest on 15 October 2026

Acknowledgement

The authors gratefully acknowledge the National Natural Science Foundation of China (31470930/C1002).

Authors' contributions

JZD and HW developed the initial concept and wrote the manuscript. JZD and YY designed the experiments. JZD and ELZ performed the experiments. JZD analysed the data. All authors discussed the results and commented on the manuscript. All authors read and approved the final manuscript.

Ethics approval and consent to participate

All animal studies were approved by the Animal Care and Use Committee of Shengjing Hospital of China Medical University and all experimental protocols were approved by the Medical and Ethics Committee of Shengjing Hospital, China Medical University, Shenyang, China.

Conflicts of interest

The authors declare that they have no competing interests.

References

1. Hodgson AWE, Kurz S, Virtanen S, Fervel V, Olsson COA, Mischler S. Passive and transpassive behaviour of CoCrMo in simulated biological solutions. *Electrochim Acta*. 2014;49:2167–78.
2. Xiang DD, Wang P, Tan XP, Chandra S, Wang C, Nai MLS, *et al*. Anisotropic microstructure and mechanical properties of additively manufactured Co–Cr–Mo alloy using selective electron beam melting for orthopedic implants. *Mater Sci Eng A Struct Mater*. 2019;765:138270. https://doi.org/10.1016/j.msea.2019.138270.
3. Igual Muñoz A, Casabán Julián L. Influence of electrochemical potential on the tibocorrosion behaviour of high carbon CoCrMo biomedical alloy in simulated body fluids by electrochemical impedance spectroscopy. *Electrochim Acta*. 2010;55:5428–39.
4. Wei D, Koizumi Y, Takashima T, Nagasako M, Chiba A. Fatigue improvement of electron beam melting-fabricated biomedical co–Cr–Mo alloy by accessible heat treatment. *Mater Res Lett*. 2018;6:93–9.
5. Shah F, Omar O, Suska F, Snis A, Matic A, Emanuelsson L, *et al*. Long-term osseointegration of 3D printed CoCr constructs with an interconnected open-pore architecture prepared by electron beam melting. *Acta Biomater*. 2016;36:296–309.
6. España FA, Balla VK, Bose S, Bandyopadhyay A. Design and fabrication of CoCrMo alloy based novel structures for load bearing implants using laser engineered net shaping. *Mater Sci Eng C Mater Biol Appl*. 2010;30:50–7.
7. Costerton JW, Stewart PS, Greenberg EP. Bacterial biofilms: a common cause of persistent infections. *Science*. 1999;284:1318–22.
8. Ribeiro M, Monteiro FJ, Ferraz MP. Infection of orthopedic implants with emphasis on bacterial adhesion process and techniques used in studying bacterial-material interactions. *Biomatter*. 2012;2:176–94.
9. Jie K, Deng P, Cao H, Feng W, Chen J, Zeng Y. Prosthesis design of animal models of periprosthetic joint infection following total knee arthroplasty: a systematic review. *PLoS One*. 2019;14:e0223402. https://doi.org/10.1371/journal.pone.0223402.
10. Ren L, Ma Z, Li M, Zhang Y, Liu W, Liao Z, *et al*. Antibacterial properties of Ti-6Al-4V-xCu alloys. *J Mater Sci Technol*. 2014;30:699–705.
11. Zhang E, Li F, Wang H, Liu J, Wang C, Li M, *et al*. A new antibacterial titanium-copper sintered alloy: preparation and antibacterial property. *Mater Sci Eng C Mater Biol Appl*. 2013;33:4280–7.
12. Liu J, Li F, Liu C, Wang H, Ren B, Yang K, *et al*. Effect of cu content on the antibacterial activity of titanium-copper sintered alloys. *Mater Sci Eng C Mater Biol Appl*. 2014;35:392–400.
13. Ren L, Wong HM, Yan CH, Yeung KWK, Yang K. Osteogenic ability of Cu-bearing stainless steel. *J Biomed Mater Res B Appl Biomater*. 2015;103:1433–44.
14. Li M, Nan L, Xu D, Ren G, Yang K. Antibacterial performance of a cu-bearing stainless steel against microorganisms in tap water. *J Mater Sci Technol*. 2015;31:243–51.
15. Xu R, Zhao M, Zhao Y, Liu L, Liu C, Gao C, *et al*. Improved biodegradation resistance by grain refinement of novel antibacterial ZK30-cu alloys produced via selective laser melting. *Mater Lett*. 2019;237:253–7.
16. Hu X, Neoh KG, Zhang J, Kang ET. Bacterial and osteoblast behavior on titanium, cobalt–chromiumalloy and stainless steel treatedwith alkali and heat: a comparative study for potential orthopedic applications. *J Colloid Interface Sci*. 2014;417:410–9.
17. Pullisaar H, Reseland JE, Haugen HJ, Brinchmann JE, Østrup E. Simvastatin coating of TiO_2 scaffold induces osteogenic differentiation of human adipose tissue-derived mesenchymal stem cells. *Biochem Bioph Res Commun*. 2014;447:139–4.
18. Zhang E, Liu C. A new antibacterial Co-Cr-Mo-Cu alloy: preparation, biocorrosion, mechanical and antibacterial property. *Mater Sci Eng C Mater Biol Appl*. 2016;69:134–43.
19. International Organization for Standardization. Implants for surgery-metallic materials-Part 4. Cobalt-chromium-molybdenum casting alloy ISO 5832-4:1996(E). 1996; Available at: https://www.iso.org/standard/23050.html.
20. Tajima K, Yamakawa M, Katagiri T, Sasaki H. Immunohistochemical detection of bone morphogenetic protein-2 and transforming growth factor beta-1 in tracheopathia osteochondroplastica. *Virchows Arch*. 1997;431:359–63.
21. Zou Y, Dong Y, Meng Q, Zhao Y, Li N. Incorporation of a skeletal muscle-specific enhancer in the regulatory region of Igf1 upregulates IGF1 expression and induces skeletal muscle hypertrophy. *Sci Rep*. 2018;8:2781. https://doi.org/10.1038/s41598-018-21122-5.
22. Exposto CR, Oz U, Westgate PM, Huja SS. Influence of miniscrew diameter and loading conditions on static and dynamic assessments of bone-implant contact: an animal study. *Orthod Craniofac Res*. 2019;22:96–100.
23. Rutten S, Nolte PA, Korstjens CM, van Duin MA, Klein-Nulend J. Low-intensity pulsed ultrasound increases bone volume, osteoid thickness and mineral apposition rate in the area

Downloaded from academic.oup.com/burnstrauma/article/doi/10.1093/burnst/tkaa036/6042489 by guest on 15 October 2026

of fracture healing in patients with a delayed union of the osteotomized fibula. *Bone*. 2008;43:348–54.
24. Bilouk S, Broussous L, Nogueira RP, Ivanova V, Pernel C. Electrochemical behavior of copper and cobalt in post-etch cleaning solutions. *Microelectron Eng*. 2009;86:2038–44.
25. Ren Z, Eppell S, Collins S, Ernst F. Co–Cr–Mo alloys: improved wear resistance through low-temperature gas-phase nitro-carburization. *Surf Coat Technol*. 2019;378: 124943. https://doi.org/10.1016/j.surfcoat.2019.124943.
26. Béreš M, Silva CC, Sarvezuk PWC, Wu L, Antunes LHM, Jardini AL, *et al*. Mechanical and phase transformation behaviour of biomedical Co-Cr-Mo alloy fabricated by direct metal laser sintering. *Mater Sci Eng A Struct Mater*. 2018;714:36–42.
27. Smith RAA, Murali S, Rai B, Lu X, Lim ZXH, Lee JJL, *et al*. Minimum structural requirements for BMP-2-binding of heparin oligosaccharides. *Biomaterials*. 2018;184:41–55.
28. Cheng ZA, Alba-Perez A, Gonzalez-Garcia C, Donnelly H, Llopis-Hernandez V, Jayawarna V, *et al*. High efficiency BMP-2 coatings: nanoscale coatings for ultralow dose BMP-2-driven regeneration of critical-sized bone defects. *Adv Sci*. 2019;6:1970009. https://doi.org/10.1002/advs.201970009.
29. Inai K, Norris RA, Hoffman S, Markwald RR, Sugi Y. BMP-2 induces cell migration and periostin expression during atrioventricular valvulogenesis. *Dev Biol*. 2008;315:383–96.
30. Rabiee A, Krüger M, Ardenkjær-Larsen J, Kahn CR, Emanuelli B. Distinct signalling properties of insulin receptor substrate (IRS)-1 and IRS-2 in mediating insulin/IGF-1 action. *Cell Signal*. 2018;47:1–15.
31. Moore DR, McKay BR, Tarnopolsky MA, Parise G. Blunted satellite cell response is associated with dysregulated IGF-1 expression after exercise with age. *Eur J Appl Physiol*. 2018;118:2225–31.
32. Bätz J, Messer-Hannemann P, Lampe F, Klein A, Püschel K, Morlock MM, *et al*. Effect of cavity preparation and bone mineral density on bone-interface densification and bone-implant contact during press-fit implantation of hip stems. *J Orthop Res*. 2019;37:1580–9.
33. Bernhardt R, Kuhlisch E, Schulz MC, Eckelt U, Stadlinger B. Comparison of bone-implant contact and bone-implant volume between 2D-histological sections and 3D-SRμCT slices. *Eur Cell Mater*. 2012;23:237–47.
34. Oest ME, Franken V, Kuchera T, Strauss J, Damron TA. Long-term loss of osteoclasts and unopposed cortical mineral apposition following limited field irradiation. *J Orthop Res*. 2015;33:334–42.
35. Isaacson BM, Potter BK, Bloebaum RD, Epperson RT, Kawaguchi B, Swanson TM, *et al*. Determining the mineral apposition rate of heterotopie ossification in military healthcare system patients after total joint replacement: a case series. *Bone Tissue Regen Insights* 2016;7:BTRI.S38041. https://doi.org/10.4137/BTRI.S38041.
36. Kawai M, Kataoka Y, Sonobe J, Yamamoto H, Maruyama H, Yamamoto T, *et al*. Analysis of mineral apposition rates during alveolar bone regeneration over three weeks following transfer of BMP-2/7 gene via in vivo electroporation. *Eur J Histochem*. 2018;62:2947. https://doi:10.4081/ejh.2018.2947.
37. Ram S. Allotropic phase transformations in HCP, FCC and BCC metastable structures in co-nanoparticles. *Mater Sci Eng A Struct Mater*. 2001;304:923–7.
38. Childress JR, Chien CL. Reentrant magnetic behavior in fcc Co-Cu alloys. *Phys Rev B*. 1991;43:8089. https://doi.org/10.1103/PhysRevB.43.8089.
39. Yamanaka K, Mori M, Chiba A. Effects of nitrogen addition on microstructure and mechanical behavior of biomedical Co–Cr–Mo alloys. *J Mech Behav Biomed Mater*. 2014;29: 417–26.
40. Li Y, Yamashita Y, Tang N, Liu B, Kurosu S, Matsumoto H, *et al*. Influence of carbon and nitrogen addition on microstructure and hot deformation behavior of biomedical Co–Cr–Mo alloy. *Mater Chem Phys*. 2012;135: 849–54.
41. Yamanaka K, Mori M, Chiba A. Effects of carbon concentration on microstructure and mechanical properties of as-cast nickel-free co–28Cr–9W-based dental alloys. *Mater Sci Eng C Mater Biol Appl*. 2014;40:127–34.
42. Bettini E, Eriksson T, Boström M, Leygraf C, Pan J. Influence of metal carbides on dissolution behavior of biomedical CoCrMo alloy: SEM, TEM and AFM studies. *Electrochim Acta*. 2011;56:9413–9.
43. Matković T, Matković P, Malina J. Effects of Ni and Mo on the microstructure and some other properties of Co-Cr dental alloys. *J Alloys Compd*. 2004; 366:293–7.
44. Issa Y, Brunton P, Waters CM, Watts DC. Cytotoxicity of metal ions to human oligodendroglial cells and human gingival fibroblasts assessed bymitochondrial dehydrogenase activity. *Dent Mater*. 2008;24:281–7.

Downloaded from academic.oup.com/burnstrauma/article/doi/10.1093/burnst/tkaa036/6042489 by guest on 15 October 2026